Low Temperature Centimeter-Scale Growth of Layered 2D SnS for Piezoelectric Kirigami Devices

Changhyeon Yoo[1], Vivek Adepu[1,2], Sang Sub Han[1], Jung Han Kim[3], June-Chul Shin[1,4], Justin Cao[1,5], Junsung Park[6], Mohammad M. Al Mahfuz[6], Laurene Tetard[1,7], Gwan-Hyoung Lee[4], Dong-Kyun Ko[6], Parikshit Sahatiya[2], Yeonwoong Jung[1,5,8]*

[1]NanoScience Technology Center, University of Central Florida, Orlando, Florida 32826, United States

[2]Department of Electrical and Electronics Engineering, Birla Institute of Technology and Science Pilani Hyderabad Campus, Hyderabad, 500078, India

[3]Department of Materials Science and Engineering, Dong-A University, Busan 49315, South Korea

[4]Department of Materials Science and Engineering, Seoul National University, Seoul 08826, South Korea

[5]Department of Materials Science and Engineering, University of Central Florida, Orlando, Florida 32816, United States

[6]Department of Electrical and Computer Engineering, New Jersey Institute of Technology, Newark, New Jersey, 07102, United States

[7]Physics Department, University of Central Florida, Orlando, Florida, 32816, United States

[8]Department of Electrical and Computer Engineering, University of Central Florida, Orlando, Florida 32816, United States

[*]Corresponding Author: yeonwoong.jung@ucf.edu

ABSTRACT: Tin monosulfide (SnS) is a promising piezoelectric material in an intrinsically layered structure, making it attractive for self-powered wearable and stretchable devices. However, for practical application purposes, it is essential to improve the output and manufacturing compatibility of SnS-based piezoelectric devices by exploring its large-area synthesis principle. In this study, we report the chemical vapor deposition (CVD) growth of centimeter-scale two-dimensional (2D) SnS layers at temperatures as low as 200 °C, allowing compatibility with processing a range of polymeric substrates. The intrinsic piezoelectricity of 2D SnS layers directly grown on polyamides (PIs) was confirmed by piezoelectric force microscopy (PFM) phase maps and force-current corroborative measurements. Furthermore, the structural robustness of the centimeter-scale 2D SnS layers/PIs allowed for engraving complicated kirigami patterns on them. The kirigami-patterned 2D SnS layer devices exhibited intriguing strain-tolerant piezoelectricity, which was employed in detecting human body motions and generating photocurrents irrespective of strain rate variations. These results establish a great promise of 2D SnS layers for practically relevant large-scale device technologies with coupled electrical and mechanical properties.

KEYWORDS: 2D layer, 2D TMD, 2D SnS, Kirigami, Piezoelectricity, Stretchable Device.

Introduction

Wearable electronics that can convert mechanical energy into electrical energy have received increasing attention in a range of technologies, such as healthcare and medical applications.[1-3] In this regard, two-dimensional (2D) materials offer distinct advantages with their ability to maintain high structural integrity under excessive mechanical stimuli owing to their large strain limits.[1, 4-8] Amongst a variety of atomically thin 2D materials, those with intrinsic piezoelectric properties are considered promising for energy harvesting applications.[9-11] Particularly, group IV 2D monochalcogenides (MXs; where M = Sn or Ge and X = S or Se) have received significant attention due to the large in-plane piezoelectricity originating from their van der Waals (vdW) hinge-like layered structure.[1, 12-14] While a large family of 2D monochalcogenides has been explored,[11] tin monosulfide (SnS) 2D layers exhibit unparalleled properties enabled by their structural anisotropy such as high piezoelectric coefficients[11] as well as ferroelectricity-driven gating[15] and synaptic characteristics.[16] Despite these appealing structure-property aspects, the centimeter-scale chemical synthesis of morphologically homogenous 2D SnS layers has been limited, hindering their practical applications.[17] For instance, direct integration of 2D SnS layers onto flexible substrates using mechanical exfoliation or liquid solution processes often leads to small-area surface coverage and uncontrolled layer morphologies.[1, 2, 18-20] Furthermore, ultrathin SnS layers synthesized from the sulfurization of metallic tin (Sn) precursors are often limited to the millimeter-scale.[21]

Herein, we report the chemical vapor deposition (CVD) growth of centimeter-scale 2D SnS layers and their piezoelectricity-driven device applications. The CVD growth was performed at a temperature as low as 200°C, which enabled their direct integration onto various polymer substrates, including polyamide (PI). Intrinsic piezoelectric properties of SnS/PIs were verified by zero-bias electrical measurements coupled with mechanical stimuli as well as piezoelectric force

microscopy (PFM). The low-temperature processability further allowed for the fabrication of SnS/PI devices with complicated kirigami and serpentine patterns, which exhibited strain-dependent piezoelectric characteristics.

Results and Discussion

In group IV 2D monochalcogenide layers, including SnS, the main polar orientation responsible for piezoelectricity is perpendicularly oriented with respect to their zigzag crystalline planes along the *c*-axis.[10, 12, 14] **Figure 1**a illustrates a schematic of tri-layered 2D SnS in an orthorhombic structure with a vdW gap spacing of 0.57 nm,[22, 23] indicating its zigzag crystallinity aligned with the *a*-axis as well as the armchair structure along the *c*-axis. **Figure 1**b illustrates the step-by-step fabrication process of 2D SnS layers-based piezoelectric devices on various substrates, including SiO_2/Si and sapphire wafers as well as PI films. The fabrication process starts with the CVD sulfurization of pre-deposited Sn thin films, which converts the Sn to 2D SnS layers. Subsequently, gold (Au) electrodes are patterned/deposited on the surface of as-grown 2D SnS layers for electrical characterizations. Details of the CVD growth conditions are presented in *Experimental Methods*. **Figure 1**c shows a camera image of samples prepared on sapphire wafers at various temperatures (left) along with a zoom-in optical microscopy image of 2D SnS layers partially grown on a sapphire wafer (right). **Figure 1**d demonstrates the scalability and patternability of this CVD growth method with 2D SnS layers grown on a large area of > 1.5 cm^2. **Figure 1**e presents images of 2D SnS layers directly grown on ~50 μm thick PI substrates with integrated Au electrodes (top), demonstrating their high mechanical flexibility (bottom).

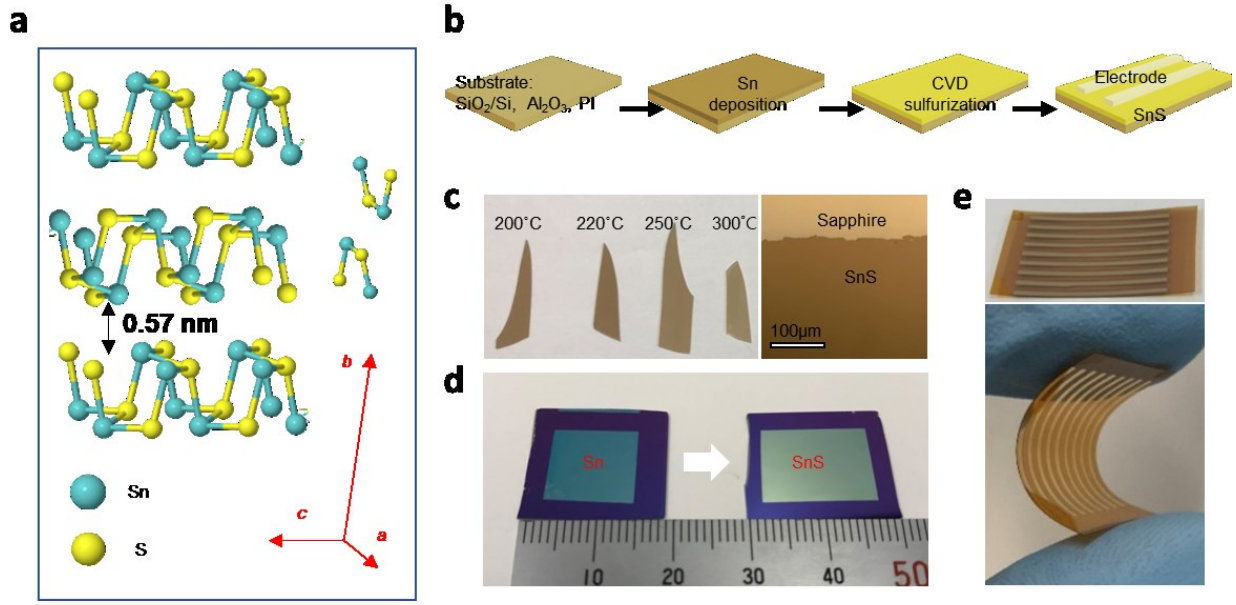

Figure 1. Growth of 2D SnS layers and their flexible device application; (a) Atomic structure illustration of orthorhombic 2D SnS layers. (b) Step-by-step procedures for the CVD growth of 2D SnS layers and their device fabrication. (c) 2D SnS layers grown on sapphire wafers prepared at various CVD temperatures. (d) Patternable and scalable growth of 2D SnS layers on SiO_2/Si wafers. (e) 2D SnS layers grown on PI substrates and their mechanical flexibility.

We comprehensively characterized the structural, chemical, and electrical properties of as-grown 2D SnS layers using various techniques; i.e., X-ray diffraction (XRD), energy-dispersive X-ray spectroscopy (EDS), transmission electron microscopy (TEM), Raman spectroscopy, X-ray Photoelectron spectroscopy (XPS), UV-visible spectroscopy, and temperature-variant electrical measurements. **Figure 2**a presents a series of XRD profiles obtained from the CVD growth performed at various temperatures. The samples prepared in a range of 200 ℃ and 300 ℃ exhibit strong peaks at 20.6 ° and 31.5 °, which correspond to the (110) and (040) planes of orthorhombic SnS (JCPDS no. 39-0354), respectively. We note that the samples prepared at 250 ℃ yield the

strongest peak intensity, while those prepared at > 300 ℃ do not exhibit characteristic peaks of SnS. Accordingly, further measurements were carried out on the samples grown at 250 ℃ unless otherwise stated. **Figure 2**b presents TEM cross-sectional EDS mapping images of 2D SnS layers grown on a sapphire wafer (i.e., crystalline Al_2O_3), revealing the highly localized distribution of Sn and S. **Figure 2**c presents the overlaid EDS line spectra corresponding to **Figure 2**b, further clarifying the high spatial homogeneity of the constituting elements. Also, the analysis determined that the thickness of the sample obtained from the CVD sulfurization of 11 nm thick Sn films is ~24 nm. **Figure 2**d presents the quantitative EDS spectrum obtained from the same sample, revealing the atomic ratio of Sn:S = 1:1. This stoichiometric growth of 2D SnS layers was further verified by XPS characterizations. **Figure 2**e displays the XPS spectrum of 2D SnS layers, presenting their Sn 3d and S 2p core-level characteristic peaks. Specifically, the core-level fitting using the Tougaard baseline reveals two doublet peaks attributed to Sn^{2+}; i.e., $3d_{3/2}$ and $3d_{5/2}$, which are obtained at the binding energy values of 493.6 eV and 485.2 eV, respectively. Furthermore, the element S 2p core-level fitting confirms the presence of two doublet peaks; i.e., $2p_{3/2}$ and $2p_{1/2}$ at 161.2 eV and 162.3 eV binding energies, respectively. The characteristic peak S $2p_{3/2}$ at 161.2 eV signifies that S is combined with Sn^{2+} to form the stoichiometric SnS, consistent with previous studies.[1, 24] **Figure 2**f displays a cross-sectional high-resolution TEM (HRTEM) image of 2D SnS layers grown on a sapphire wafer, which reveals a measured lattice spacing of 0.57 nm corresponding to (020) lattice fringes. The overlay image depicts a simulated atomic structure model presenting (020) lattice fringes, confirming the orthorhombic structure consistent with previous studies.[25-27] Additionally, the surface roughness of the 2D SnS layers grown on a sapphire wafer was characterized with atomic force microscopy (AFM), as presented **in Supporting Information Figure S1,** where the root-mean-squared (Rms) roughness of the scanned area (10 ×

10 μm^2) is around 3.42 nm. **Figure 2**g presents Raman characterization results, revealing characteristic Raman peaks at ~ 94.7 cm^{-1}, 158.1 cm^{-1}, 185.4 cm^{-1}, and 222.4 cm^{-1}. These values are assigned to the various vibration modes of A_g and B_{3g} for 2D SnS layers, fully consistent with previous studies.[23, 28-31] We also note that un-optimized samples (e.g., grown at a higher temperature) often exhibit additional peaks at 309.2 cm^{-1} that are indicative of residual SnS_2 phases,[32] which can be eliminated through a post-annealing process (**Supporting Information**, **Figure S2**). **Figure 2**h shows the UV-visible absorbance spectrum for 2D SnS layers directly grown on a glass substrate, along with the corresponding optical microscopy image (inset). **Figure 2**i presents the corresponding Tauc plot of $(\alpha hv)^{1/2}$ vs. hv converted from the absorbance spectrum, where α is the optical absorption coefficient and hv is the photon energy.[6] The extrapolation of the Tauc plot reveals that the optical bandgap energy of 2D SnS layers is in a range of ~1.0–1.1 eV, which agrees well with previous studies.[33, 34] The semiconducting characteristics of 2D SnS layers were further verified by temperature-variant electrical characterizations. **Figure 2**j presents the temperature-dependent increase of electrical conductivity obtained from the two-terminal current-voltage (I–V) measurements with Ohmic transports in a range of 300–550K (**Supporting Information**, **Figure S3**). The results indicate the dominant contribution of thermally-excited free carriers in 2D SnS layers, further confirming their semiconducting nature. The carrier type of the semiconducting 2D SnS layers was identified by field effect transistor (FET) characterizations, which revealed *p*-type transport characteristics, as presented in **Supporting Information, Figure S4.** Previous studies report that 2D SnS layers generally exhibit *p*-type semiconductor characteristics at room temperature, consistent with our observations, which is attributed to the presence of Sn vacancies that act as shallow acceptors.[35]

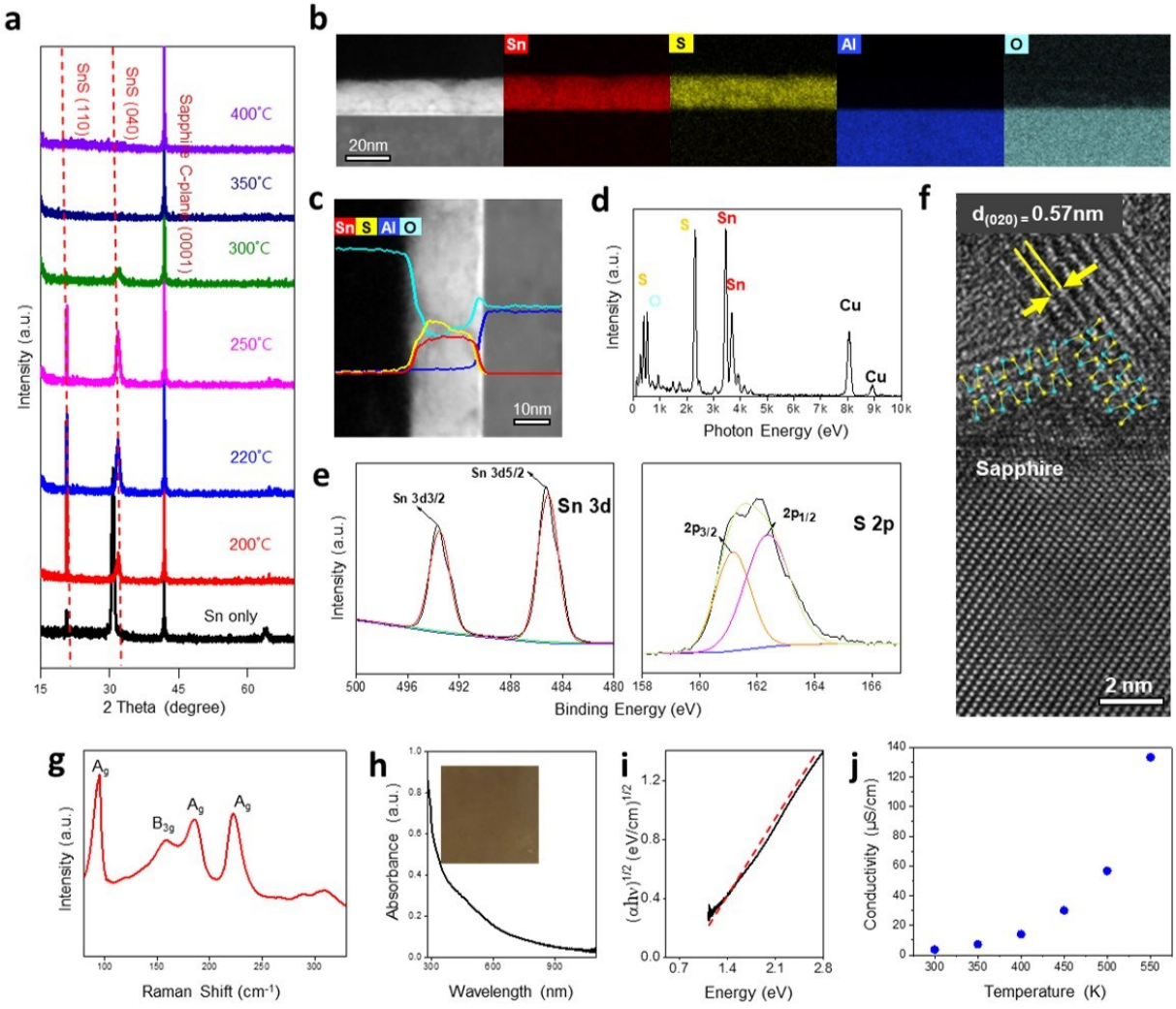

Figure 2. Characterizations of CVD-grown 2D SnS layers; (a) XRD profiles acquired at varying temperatures of 200 ℃ to 400 ℃. (b) Cross-sectional EDS elemental mapping images of 2D SnS layers. (c) EDS line profile corresponding to (b). (d) EDS spectrum corresponding to (b). (e) High-resolution core-level fitted XPS spectra for Sn 3d (left) and S 2p (right). (f) Cross-sectional HRTEM of 2D SnS layers. (g) Raman spectrum of 2D SnS layers. (h) UV-vis absorbance spectrum of 2D SnS layers. (i) Tauc plot corresponding to (h). (j) Temperature-dependent electrical conductivity.

Following the comprehensive characterizations, we investigated the piezoelectric response of SnS/PI samples by simultaneously measuring their current change under a period application of force loads. **Figure 3**a displays the corresponding force-current responses measured at a zero bias, acquired with a motorized force tester (Mark-10 ESM303). The plot presents both the input of "force per time" (blue) and the output of "current response" (red), as well as a zoom-in view of the current increase/decrease following the periodic trend of the load application/release. The maximum current peaks were observed to coincide with the maximum force per time peaks. The maximum current values of ~ -2.19 nA and ~1.27 nA were generated while the compressive force was applied (83.29 N/s) and released (-42 N/s), respectively, wherein all these values were averaged for 12 cycles of compression/release. The circular compression plate (area = ~1.77 cm^2) subject to the force loading was covered by PI tape for current leak prevention, as shown in the inset of **Figure 3**a (top right). The tested SnS/PI device (2 cm × 1.5 cm) with interdigitated Au electrodes is shown in the inset of **Figure 3**a (right bottom). **Figure 3**b presents current temporal responses obtained under varying force load amounts, revealing the piezoelectric currents of 0.25 nA, 1.85 nA, and 2.57 nA corresponding to the compression/release pressures of 11.3 kPa, 28.3 kPa, and 55.6 kPa, respectively. **Figure 3**c shows the corresponding plot of applied pressure vs. generated current, revealing the increasing trend of current values with increasing pressures. After these mechano-electrical characterizations, we employed piezoelectric force microscopy (PFM) to determine the local piezoelectric contribution of 2D SnS layers. **Figure 3**d presents the PFM amplitude (left) and phase (right) images of a sample prepared on an Au contact deposited-SiO_2/Si wafer, which were obtained from a scanning area of 10 × 10 μm^2. The PFM amplitude image reflects the topography of the three-dimensional SnS surface morphology, revealing its high spatial homogeneity consistent with the low Rms value of surface roughness in **Supporting Information,**

Figure S1. The high homogeneity of the PFM amplitude contrast indicates the small size of individual 2D SnS layer grains, which is revealed to be around ~20 nm by plane-view TEM characterizations (**Supporting Information, Figure S5**). The PFM phase image corresponding to the amplitude image was also obtained to identify the polarization distribution of piezoelectric domains within the sample, which is to be magnified by PFM phase contrast. While the image displays a homogeneous distribution of discernible phase contrast, it is challenging to clearly quantify/distinguish the polarizing domains due to the small grain size. To mitigate the challenge, we then explored the quantitative correlation of the PFM amplitude and phase by obtaining their characteristic spectra. **Figure 3**e and f show the spectra of the correlated PFM amplitude and phase, respectively, as a function of a bias voltage applied to the sample, which was obtained under a DC bias sweep in the direction of $0 \rightarrow 5 \rightarrow 0 \rightarrow -5 \rightarrow 0$V. The PFM tip driving voltage was 10 V with respect to the bottom Au film on the sample, which was directly contacted with copper electrodes. The observation of the amplitude butterfly loop (i.e., piezoelectric hysteresis) in **Figure 3**e and the 180 ° phase difference in **Figure 3**f with respect to the applied bias strongly confirms the intrinsic piezoelectricity of 2D SnS layers. The presented data are the average values of those obtained from 10 different locations of the sample. Schematics of the PFM sample preparation as well as an image of the tested sample, are presented in **Supporting Information, Figure S6.** The PFM amplitude spectrum depicts a butterfly-shaped loop with a somewhat reduced prominence compared to mechanically exfoliated SnS flakes.[15] This slight signal reduction can be attributed primarily to the tilted orientation of CVD SnS layers, where the signal was measured using a vertical PFM. However, the PFM phase exhibits a significant 180 ° phase difference relative to the applied DC bias, indicating robust piezoelectric characteristics. These PFM results are fully consistent with previous measurements using mechanically exfoliated 2D SnS layers of much

smaller lateral dimensions (typically < 1 μm^2).[15] PFM images in a three-dimensional projected view are also presented in **Supporting Information**, **Figure S7**. Furthermore, we employed ultraviolet photoelectron spectroscopy (UPS) and investigated the charge transport nature of 2D SnS layers/Au electrodes to ensure the pressure-driven current responses are intrinsic characteristics of 2D SnS layers. (**Supporting Information**, **Figure S8**). The work function of *p*-type semiconducting 2D SnS layers is determined to be 5.04 eV (**Supporting Information**, **Figure S8**a), which leads to good ohmic transports once they are interfaced with Au of a larger work function (**Supporting Information, Figure S8**b). Accordingly, the influences of Schottky barrier heights at the SnS/Au heterojunctions on resulting electrical responses will not be significant. When the Au-contacted 2D SnS layers are subjected to pressures, a certain extent of their zigzag crystalline planes will be aligned to the orientation of the exerted pressures due to the nature of their mixed layer orientations (**Figure 2**f), which results in considerable piezoresponses.

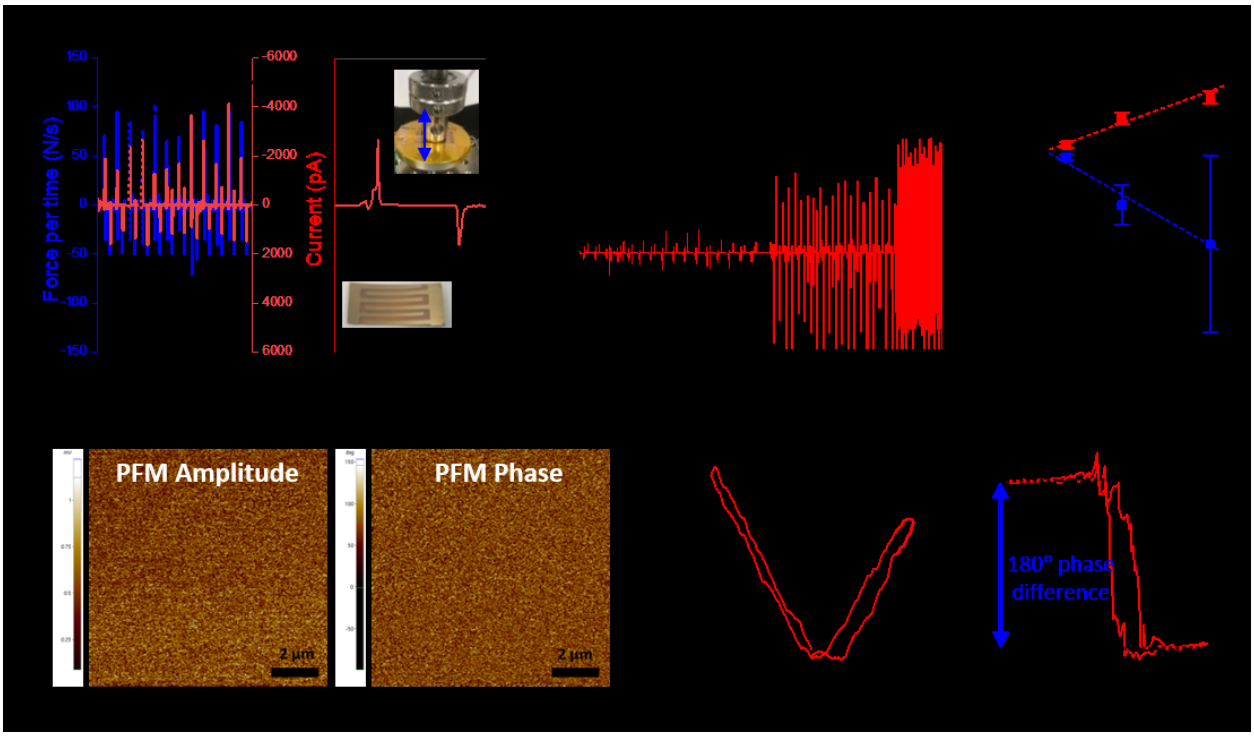

Figure 3. Piezoelectricity demonstration at the macro- and nano-scale with PFM; (a) Representation of the force as a function of time (blue, left axis) and its corresponding current output (red, right axis). The zoom-in view presents the current responses corresponding to the first application cycle of the force per time input. (b) Evolution of current generation with increasing pressure values. (c) Correlation of applied pressure vs. generated current corresponding to (b). (d) PFM images of amplitude (left) and phase (right) obtained with a tip bias of 10V. (e, f) PFM spectra of (e) amplitude and (f) phase obtained during the DC bias sweep in the direction of 0 → 5 → 0 → -5 → 0V.

Having confirmed the material quality and the intrinsic piezoelectricity of 2D SnS layers, we then pursued their device applications, particularly by focusing on skin-attachable physical sensors that can detect human body motions.[2, 19] In this context, it is recommended that these sensors exhibit a maximum stretchability of at least 70%, which is to ensure their conformal integration

onto any parts of human bodies.[20, 36] Herein, we explored kirigami-patterned piezoelectric sensors by combining the intrinsic piezoelectricity of 2D SnS layers with the controllability of strain tolerance enabled by kirigami patterns. We fabricated the sensors by directly engraving kirigami patterns of pre-defined dimensions onto 2D SnS layers-grown PI substrates using a mechanical cutter (Cricut Explore Air 2, Cricut, Inc., USA).[18, 37] **Figure 4**a illustrates a schematic of the fabrication process of the kirigami-patterned 2D SnS layers/PI device with cutting dimensions of a = 11.25 mm, b = 1.5 mm, and c = 1.5 mm within a typical sensor dimension of 15 mm × 15 mm (excluding Au electrode regions). **Figure 4**b shows an image of an SnS/PI kirigami sensor in stretching motions with increasing tensile strains from 0 to 200%. **Figure 4**c shows *I–V* characteristics of another sample under systematically increasing tensile strains up to 140 % with a step of 20 %. While the kirigami sensor well maintains its mechanical robustness even under the elongated stretching – to be verified in the next section – we note that it exhibits a noticeable current drop per each stretching cycle – i.e., about 0.3 % current decrease per 20% strain. This observation indicates that the SnS/PI kirigami device still experiences a considerable extent of an instant accumulation of strain during the operation despite its large overall stretchability, which is utilized to generate piezoelectricity. **Figure 4**d presents current temporal responses obtained from the sample in **Figure 4**b periodically undergoing stretching to 100% for ~1.5 seconds, followed by its release to the unstretched state after ~3.5 seconds (strain rate = 10 mm/s). The kirigami sensor exhibits highly uniform current values only during the stretching/release periods, reflecting its strain-driven piezoelectricity, while no current is generated when it is not in motion, as clarified in the zoom-in view. **Figure 4**e compares the current generation characteristics obtained during two different tensile stretching events; i.e., from 0 to 100 % strain (top) vs. from 100 to 200 % strain (bottom) for 3 seconds under an identical strain rate. Similar characteristics are observed

for both cases involving a 100% strain increase over the original states, consistent with the *I-V* characteristics in **Figure 4**c. The corresponding movie of the uni-directionally stretching SnS/PI kirigami device is provided in **Supporting Information, Video S1.** **Figure 4**f compares the average of maximum current values obtained during the stretch (left) and release (right) events corresponding to **Figure 4**e, further revealing similar current generation characteristics. To further demonstrate the versatility of this kirigami design approach in obtaining strain-driven piezoelectric characteristics, we developed serpentine-patterned SnS/PI piezoelectric devices capable of multi-directional stretching.[38, 39] **Figure 4g** presents camera images of a serpentine-patterned SnS/PI device progressively undergoing bi-directional stretching up to 100% strain. The serpentine-patterned arms are connected to the central common area, while their four ends are connected to metal electrodes for electrical measurements. **Figure 4h** illustrates the piezoelectric current generation from the device undergoing 10 stretch/relax cycles measured in x- (left) and y- (right) directions with a varying strain rate of 50% to 100%. It is observed that the amount of the generated current is similar irrespective of the strain rate variation, consistent with the characteristics observed with the uni-directionally stretchable kirigami device. The corresponding video of the bi-directionally stretching device is presented in **Supporting Information, Video S2.** Note that all the piezoelectric measurements were performed under zero bias conditions, confirming that the kirigami device's self-powering ability accompanying a large mechanical stretchability is suitable for human motion detections.

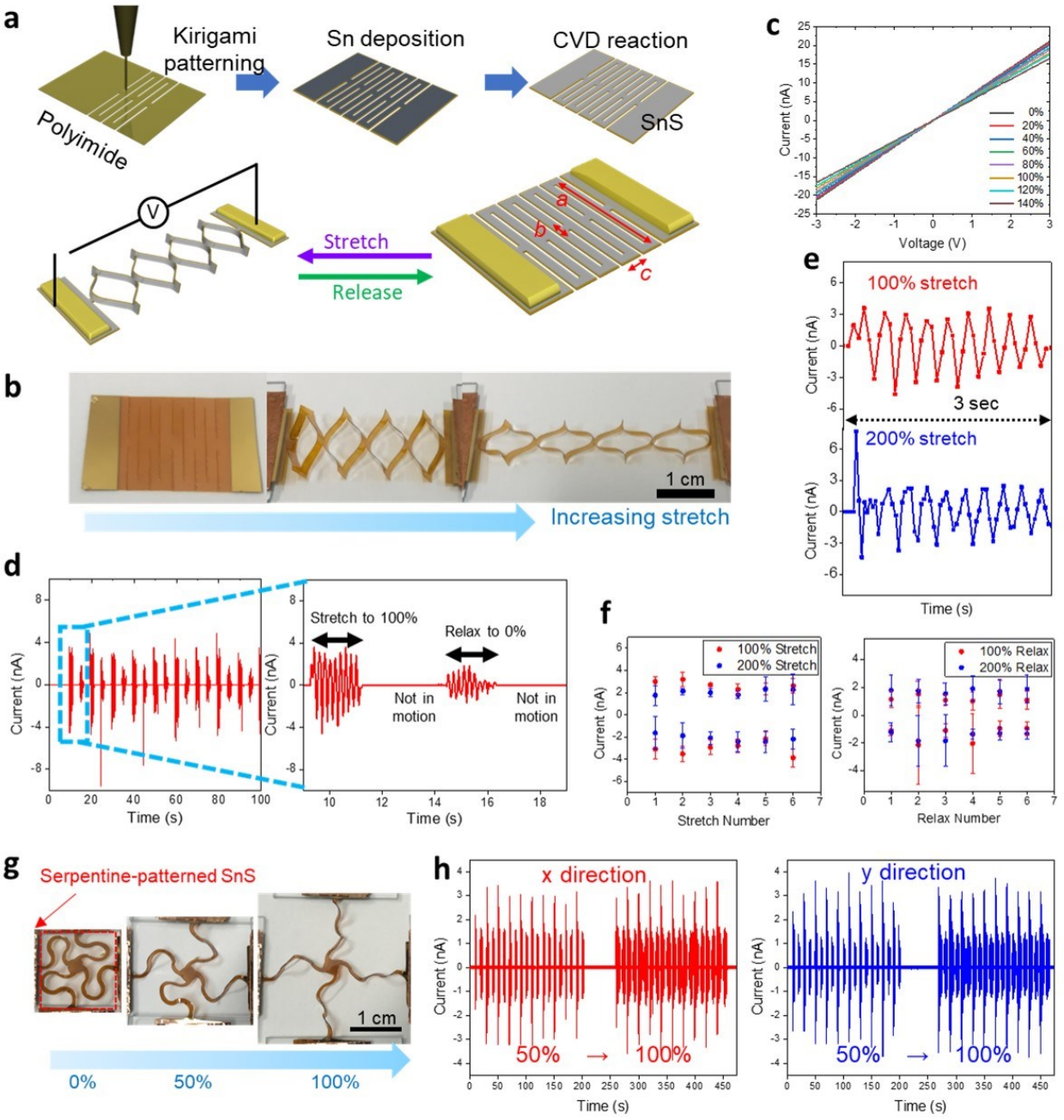

Figure 4. Demonstration of kirigami-patterned piezoelectric SnS/PI devices operations and their strain-dependent current generation characteristics; (a) Schematics illustrating the step-by-step fabrication process of SnS/PI kirigami devices. (b) Images of a SnS/PI kirigami device progressively undergoing tensile stretching. (c) Strain-dependent *I–V* characteristics of a SnS/PI kirigami device. (d) Temporal response plots of the same device under a periodic 100 % stretch

and relax. (e) Temporal response plots of the same device during 100 % (top) and 200 % (bottom) stretches. (f) Generated current values vs. stretch (left) and relax (right) numbers for 100 % and 200 % tests. (g) Camera images of a serpentine-patterned SnS/PI piezoelectric device undergoing bi-directional stretching. (h) Current generation by 50 % and 100 % stretch/relax for 10 cycles in each x- and y-direction.

We then explored application aspects of SnS/PI kirigami devices by taking advantage of their large lateral stretchability coupled with strain-driven current generation. To verify their versatility, we demonstrated the reversibility of their current generation driven by human motions (**Figure 5a-5c**) and light illuminations (**Figure 5d**). For proof-of-concept human motion detection, we attached a SnS/PI kirigami device to various parts of human bodies and monitored its current generation driven by their movements. **Figure 5**a demonstrates the current generation of the kirigami sensor driven by the bending/release motions of a wrist (left), a finger (middle), and an elbow (right). **Figure 5**b presents the piezoelectric response of the same sample attached to a foot, which exerts pressures in up/down directions. The sensor was tested for > 2 min, during which no performance degradation was observed, indicating the structural robustness of 2D SnS layers. **Figure 5**c demonstrates the walking (left) and running (right) -driven generation of zero-bias currents, which further emphasizes the excellent adaptability and reliability of the sensor. Furthermore, we explored the photocurrent generation ability of SnS/PI kirigami devices at various tensile stretching levels. **Figure 5**d inset shows an optical image (top) of a 100% stretched-kirigami device exposed to an illuminating LED (Thorlabs M625L4-C2) with a wavelength of 625 nm and an intensity of 22 W m^{-2}. The plot presents the temporal normalized photocurrent response of the

same device with varying stretch levels measured at 5V bias, revealing the photon energy-inducted current generation (ON state) and elimination (OFF state). Lastly, we tested the mechanical robustness of SnS/PI kirigami devices under extreme operation conditions involving a large number of stretch/relax cycles for 3000 seconds. **Figure 5e** shows the constant generation of piezoelectric current during the course of 150 cycles at a fixed strain rate of 100 %, confirming their excellent mechanical robustness.

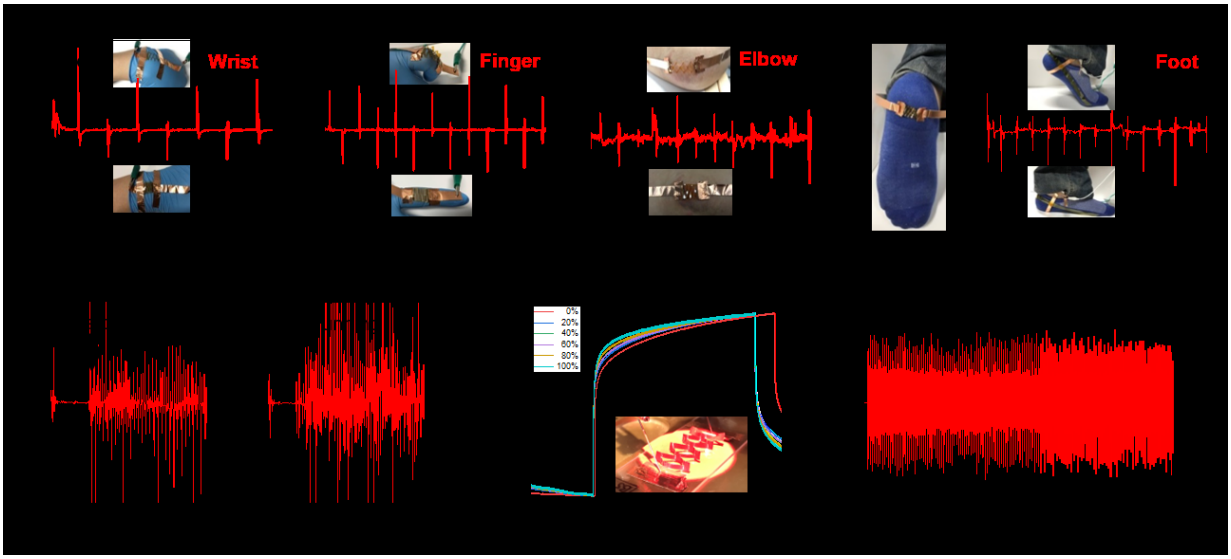

Figure 5. Various applications of SnS/PI kirigami devices; (a), (b) Temporal response plots of an identical device attached to a human body at various positions, such as; (a) wrist, finger, elbow, and (b) foot. (c) Temporal response plots obtained during walking and running. (d) Photocurrent measurement demonstration (inset) and its corresponding temporal normalized photocurrent generation with varying strain rates. (e) Current generation during stretch/relax cycles for 3000 seconds at a fixed strain rate of 100%.

Conclusions

In summary, we explored the scalable and patternable growth of piezoelectric 2D SnS layers at a CVD reaction temperature as low as 200 °C, making it compatible with the process temperature of various polymeric substrates. Their direct integration onto PI substrates and subsequent kirigami patterning enabled the fabrication of skin-attachable sensor devices, which can accommodate a large degree of multi-directional stretching coupled with the strain-controlled generation of piezoelectric currents. The intrinsic piezoelectricity of the centimeter-scale 2D SnS layers was thoroughly verified by combining corroborative mechano-electrical measurements and PFM characterizations. This study suggests an excellent manufacturing processability of atomically thin piezoelectric materials, which can be integrated onto substrates of unrestricted physical forms, allowing for device operations in various form factors.

Experimental Methods

CVD growth of 2D SnS layers on various substrates. Sn seed films with controlled thickness were deposited onto various substrates, including SiO_2/Si wafers, sapphire wafers, and PI films, using an electron beam evaporator (Temescal FC-2000). The deposition was conducted at a rate of ~1 Å/sec and a chamber base pressure of $<5.5\times10^{-7}$ Torr. The Sn-deposited substrates were placed in the center of a quartz tube inside a CVD thermal furnace (Blue M Mini-Mite, Lindberg) along with S powders (CAS No. 7704-34-9, Product No. 215198, reagent grade, 100 mesh, ≥99.5%, Sigma-Aldrich) in an alumina boat at the upstream side of the furnace. The CVD chamber was then pumped down to <50 mTorr and ultra-pure Ar gas was introduced at a rate of 100 standard cubic centimeters per minute (SCCM) to maintain an operating pressure of ~110 mTorr during the

CVD process. In 20 minutes, the CVD furnace was heated to 250°C and was kept at that temperature for 50 minutes before being allowed to cool down to room temperature naturally.

Characterizations using TEM, XRD, Raman, UV-Vis, and PFM. All TEM characterizations, including HR-TEM and EDS, were performed using FE-STEM Talos F200X G2 (Thermo Fisher Scientific) operated at an acceleration voltage of 200 kV. For sample preparation of the cross sections for TEM, standard focus ion beam lift-out techniques were employed. XRD measurements (PANalytical, X'pert PRO-XPD) were carried out using Cu Kα radiation of 1.54 Å. Raman spectra were acquired using Horiba LabRAM HR Evolution at room temperature with a 532 nm excitation laser, laser power of 1%, acquisition time of 1 second, accumulation of 10, and 1800 grating. PFM images were acquired using a Park NX10 AFM (Park systems, Corp.) with off-resonance PFM (OR PFM) settings with 17 kHz of 10 V AC bias applied to a conductive PPP-EFM (Nanosensors^{TM}) probe. Optical absorbance spectra were obtained by UV-Vis spectroscopy (Evolution 220 UV-vis spectrometer) in a wavelength range of 200–1100 nm.

Temperature-dependent conductivity measurement. Samples for temperature-dependent electrical conductivity measurements were fabricated by depositing Au contacts to as-grown SnS layers (channel length: 0.2 cm, channel width: 0.8 cm, and film thickness: 21 nm). The formation of ohmic contacts was confirmed by the linearity of *I–V* plots measured up to $\pm$10V. All measurements were conducted using Agilent 4155A with the sample temperature controlled by MMR variable temperature chamber coupled with K2000 temperature controller.

Supporting Information

AFM characterizations of the surface roughness of 2D SnS layers, Raman spectra of 2D SnS layers before/after H_2(10%)/Ar (90%) mixture gas annealing at 350°C for 5 mins, FET characterizations of 2D SnS layers, Schematics/images of PFM sample preparation, Three dimensionally-projected PFM images (topography, amplitude, and phase), UPS measurements and energy band diagrams, Image of serpentine-patterned kirigami preparation (PDF). Videos demonstrating the uni-directional and bi-directional stretching of SnS/PI kirigami devices.

Author Information

Corresponding Author

*Yeonwoong Jung – NanoScience Technology Center and Department of Materials Science and Engineering, University of Central Florida, Orlando, Florida 32826, United States; Email: yeonwoong.jung@ucf.edu

Author Contributions

C.Y. conceived the project idea under the guidance of Y.J. C.Y. prepared samples and performed piezoelectric tests under the guidance of Y.J. V.A., S.S.H., J.-C.S., and J.C. assisted in the sample preparation and characterization under the guidance of L.T., G.-H.L., and Y.J. J.H.K performed the structural characterization of samples. J.P., M.M.A.M., and D.-K. K performed temperature-dependent conductivity measurements. C.Y. and Y.J. wrote the manuscript with inputs from all authors.

Notes

The authors declare no competing financial interests.

Acknowledgments

Y.J. acknowledges financial support from the US National Science Foundation (CAREER: 2142310). G.H.L. acknowledges the support from the National Research Foundation (NRF) of Korea Grant funded by the Korean Government (2021R1A2C3014316), the Research Institute of Advanced Materials (RIAM), Institute of Engineering Research (IER), Institute of Applied Physics (IAP), and Inter-University Semiconductor Research Center (ISRC) at the Seoul National University. J.H.K acknowledges the support from the Ministry of Science and ICT (Project Number: (2023) 2023-22030006-00) and the Commercialization Promotion Agency for R&D Outcomes (COMPA).

References

(1) Khan, H.; Mahmood, N.; Zavabeti, A.; Elbourne, A.; Rahman, M. A.; Zhang, B. Y.; Krishnamurthi, V.; Atkin, P.; Ghasemian, M. B.; Yang, J.; et al. Liquid metal-based synthesis of high performance monolayer SnS piezoelectric nanogenerators. *Nat. Commun.* **2020**, *11* (1), 3449

(2) Sun, R.; Carreira, S. C.; Chen, Y.; Xiang, C.; Xu, L.; Zhang, B.; Chen, M.; Farrow, I.; Scarpa, F.; Rossiter, J. Stretchable Piezoelectric Sensing Systems for Self-Powered and Wireless Health Monitoring. *Adv. Mater. Technol.* **2019**, *4* (5), 1900100

(3) Dulal, M.; Afroj, S.; Ahn, J.; Cho, Y.; Carr, C.; Kim, I.-D.; Karim, N. Toward Sustainable Wearable Electronic Textiles. *ACS Nano* **2022**, *16* (12), 19755-19788

(4) Yoo, C.; Yoon, J.; Kaium, M. G.; Osorto, B.; Han, S. S.; Kim, J. H.; Kim, B. K.; Chung, H.-S.; Kim, D.-J.; Jung, Y. Large-area vertically aligned 2D MoS_2 layers on TEMPO-cellulose nanofibers for biodegradable transient gas sensors. *Nanotechnology* **2022**, *33* (47), 475502

(5) Yoo, C.; Han, S. S.; Okogbue, E.; Bae, T.-S.; Jang, J. H.; Cao, J.; Chung, H.-S.; Jung, Y. Humidity-Driven High-Performance Electrothermal Actuation of Vertically Stacked 2D $PtTe_2$ Layers/Cellulose Nanofibers. *Adv. Intell. Syst.* **2023**, *5* (3), 2200269

(6) Yoo, C.; Ko, T.-J.; Han, S. S.; Shawkat, M. S.; Oh, K. H.; Kim, B. K.; Chung, H.-S.; Jung, Y. Mechanically rollable photodetectors enabled by centimetre-scale 2D MoS_2 layer/TOCN composites. *Nanoscale Adv.* **2021**, *3* (11), 3028-3034

(7) Ko, T.-J.; Wang, M.; Yoo, C.; Okogbue, E.; Islam, M. A.; Li, H.; Shawkat, M. S.; Han, S. S.; Oh, K. H.; Jung, Y. Large-area 2D TMD layers for mechanically reconfigurable electronic devices. *J. Phys. D: Appl. Phys.* **2020**, *53* (31), 313002

(8) Akinwande, D.; Brennan, C. J.; Bunch, J. S.; Egberts, P.; Felts, J. R.; Gao, H.; Huang, R.; Kim, J.-S.; Li, T.; Li, Y.; et al. A review on mechanics and mechanical properties of 2D materials—Graphene and beyond. *Extreme Mech. Lett.* **2017**, *13*, 42-77

(9) Cao, V. A.; Kim, M.; Hu, W.; Lee, S.; Youn, S.; Chang, J.; Chang, H. S.; Nah, J. Enhanced Piezoelectric Output Performance of the SnS_2/SnS Heterostructure Thin-Film Piezoelectric Nanogenerator Realized by Atomic Layer Deposition. *ACS Nano* **2021**, *15* (6), 10428-10436

(10) Gomes, L. C.; Carvalho, A.; Castro Neto, A. H. Enhanced piezoelectricity and modified dielectric screening of two-dimensional group-IV monochalcogenides. *Phys. Rev. B* **2015**, *92* (21), 214103

(11) Fei, R.; Li, W.; Li, J.; Yang, L. Giant piezoelectricity of monolayer group IV monochalcogenides: SnSe, SnS, GeSe, and GeS. *Appl. Phys. Lett.* **2015**, *107* (17), 173104

(12) Wu, M.; Zeng, X. C. Intrinsic Ferroelasticity and/or Multiferroicity in Two-Dimensional Phosphorene and Phosphorene Analogues. *Nano Lett.* **2016**, *16* (5), 3236-3241

(13) Wang, H.; Qian, X. Two-dimensional multiferroics in monolayer group IV monochalcogenides. *2d Mater.* **2017**, *4* (1), 015042

(14) Bao, Y.; Song, P.; Liu, Y.; Chen, Z.; Zhu, M.; Abdelwahab, I.; Su, J.; Fu, W.; Chi, X.; Yu, W.; et al. Gate-Tunable In-Plane Ferroelectricity in Few-Layer SnS. *Nano Lett.* **2019**, *19* (8), 5109-5117

(15) Singh, P.; Rhee, D.; Baek, S.; Yoo, H. H.; Niu, J.; Jung, M.; Kang, J.; Lee, S. SnS/MoS_2 van der Waals heterojunction for in-plane ferroelectric field-effect transistors with multibit memory and logic characteristics. *EcoMat* **2023**, *5* (5), e12333

(16) Kwon, K. C.; Zhang, Y.; Wang, L.; Yu, W.; Wang, X.; Park, I.-H.; Choi, H. S.; Ma, T.; Zhu, Z.; Tian, B.; et al. In-Plane Ferroelectric Tin Monosulfide and Its Application in a Ferroelectric Analog Synaptic Device. *ACS Nano* **2020**, *14* (6), 7628-7638

(17) Sutter, P.; Komsa, H. P.; Lu, H.; Gruverman, A.; Sutter, E. Few-layer tin sulfide (SnS): Controlled synthesis, thickness dependent vibrational properties, and ferroelectricity. *Nano Today* **2021**, *37*, 101082

(18) Ko, T.-J.; Han, S. S.; Okogbue, E.; Shawkat, M. S.; Wang, M.; Ma, J.; Bae, T.-S.; Hafiz, S. B.; Ko, D.-K.; Chung, H.-S.; et al. Wafer-scale 2D $PtTe_2$ layers-enabled Kirigami heaters with superior mechanical stretchability and electro-thermal responsiveness. *Appl. Mater. Today* **2020**, *20*, 100718

(19) Xu, K.; Lu, Y.; Honda, S.; Arie, T.; Akita, S.; Takei, K. Highly stable kirigami-structured stretchable strain sensors for perdurable wearable electronics. *J. Mater. Chem. C* **2019**, *7* (31), 9609-9617

(20) Kim, H.; Seo, M.; Kim, J.-W.; Kwon, D.-K.; Choi, S.-E.; Kim, J. W.; Myoung, J.-M. Highly Stretchable and Wearable Thermotherapy Pad with Micropatterned Thermochromic Display Based on Ag Nanowire–Single-Walled Carbon Nanotube Composite. *Adv. Funct. Mater.* **2019**, *29* (24), 1901061

(21) Krishnamurthi, V.; Khan, H.; Ahmed, T.; Zavabeti, A.; Tawfik, S. A.; Jain, S. K.; Spencer, M. J. S.; Balendhran, S.; Crozier, K. B.; Li, Z.; et al. Liquid-Metal Synthesized Ultrathin SnS Layers for High-Performance Broadband Photodetectors. *Adv. Mater.* **2020**, *32* (45), 2004247

(22) Choi, H.; Lee, N.; Park, H.; Choi, Y.; Kim, K.; Choi, Y.; Kim, J.; Song, S.; Yuk, H.; Jeon, H. Development of a SnS Film Process for Energy Device Applications. *Appl. Sci.* **2019**, *9* (21),

(23) Xia, J.; Li, X.-Z.; Huang, X.; Mao, N.; Zhu, D.-D.; Wang, L.; Xu, H.; Meng, X.-M. Physical vapor deposition synthesis of two-dimensional orthorhombic SnS flakes with strong angle/temperature-dependent Raman responses. *Nanoscale* **2016**, *8* (4), 2063-2070

(24) Zhang, Y.; Guo, B.; Hu, L.; Xu, Q.; Li, Y.; Liu, D.; Xu, M. Synthesis of SnS nanoparticle-modified MXene ($Ti_3C_2T_x$) composites for enhanced sodium storage. *J. Alloys Compd.* **2018**, *732*, 448-453

(25) Patel, M.; Kim, H.-S.; Kim, J. Wafer-scale production of vertical SnS multilayers for high-performing photoelectric devices. *Nanoscale* **2017**, *9* (41), 15804-15812

(26) Gou, X.-L.; Chen, J.; Shen, P.-W. Synthesis, characterization and application of SnS_x (x=1, 2) nanoparticles. *Mater. Chem. Phys.* **2005**, *93* (2), 557-566

(27) Shriber, P.; Avraham, E. S.; Malik, B.; Teblum, E.; Girshevitz, O.; Perelshtein, I.; Ejgenberg, M.; Gofer, Y.; Zubarev, Y.; Nagler, P.; et al. Controlling the morphology while retaining the unique SnS stoichiometry of bulk tin sulfide produced by the rapid method of heating Sn foil in sulfur vapor by vapor phase reaction using two-furnace chemical vapor deposition system. *Chem. Pap.* **2023**, *77* (3), 1273-1286

(28) Lu, X. F.; Zhang, Y.; Wang, N.; Luo, S.; Peng, K.; Wang, L.; Chen, H.; Gao, W.; Chen, X. H.; Bao, Y.; et al. Exploring Low Power and Ultrafast Memristor on p-Type van der Waals SnS. *Nano Lett.* **2021**, *21* (20), 8800-8807

(29) Felton, J.; Blundo, E.; Kudrynskyi, Z.; Ling, S.; Bradford, J.; Pettinari, G.; Cooper, T.; Wadge, M.; Kovalyuk, Z.; Polimeni, A.; et al. Hydrogen-Induced Conversion of SnS_2 into SnS or Sn: A Route to Create SnS_2/SnS Heterostructures. *Small* **2022**, *18* (33), 2202661

(30) Li, M.; Wu, Y.; Li, T.; Chen, Y.; Ding, H.; Lin, Y.; Pan, N.; Wang, X. Revealing anisotropy and thickness dependence of Raman spectra for SnS flakes. *RSC Adv.* **2017**, *7* (77), 48759-48765

(31) Higashitarumizu, N.; Kawamoto, H.; Nakamura, M.; Shimamura, K.; Ohashi, N.; Ueno, K.; Nagashio, K. Self-passivated ultra-thin SnS layers via mechanical exfoliation and post-oxidation. *Nanoscale* **2018**, *10* (47), 22474-22483

(32) Lee, N.; Bang, M.; Choi, H.; Park, H.; Lee, S. G.; Lee, E. J.; Jeon, H. Effect of H2 annealing on SnS thin films grown by thermal evaporation and their transfer characteristics with Ti, W, and Mo electrodes. *Thin Solid Films* **2021**, *732*, 138779

(33) Ballipinar, F.; Rastogi, A. C. Tin sulfide (SnS) semiconductor photo-absorber thin films for solar cells by vapor phase sulfurization of Sn metallic layers using organic sulfur source. *J. Alloys Compd.* **2017**, *728*, 179-188

(34) Tanuševski, A.; Poelman, D. Optical and photoconductive properties of SnS thin films prepared by electron beam evaporation. *Sol. Energy Mater. Sol. Cells* **2003**, *80* (3), 297-303

(35) Tian, Z.; Guo, C.; Zhao, M.; Li, R.; Xue, J. Two-Dimensional SnS: A Phosphorene Analogue with Strong In-Plane Electronic Anisotropy. *ACS Nano* **2017**, *11* (2), 2219-2226

(36) Ní Annaidh, A.; Bruyère, K.; Destrade, M.; Gilchrist, M. D.; Otténio, M. Characterization of the anisotropic mechanical properties of excised human skin. *J. Mech. Behav. Biomed. Mater.* **2012**, *5* (1), 139-148

(37) Okogbue, E.; Han, S. S.; Ko, T.-J.; Chung, H.-S.; Ma, J.; Shawkat, M. S.; Kim, J. H.; Kim, J. H.; Ji, E.; Oh, K. H.; et al. Multifunctional Two-Dimensional $PtSe_2$-Layer Kirigami Conductors with 2000% Stretchability and Metallic-to-Semiconducting Tunability. *Nano Lett.* **2019**, *19* (11), 7598-7607

(38) Han, S. S.; Ko, T.-J.; Shawkat, M. S.; Shum, A. K.; Bae, T.-S.; Chung, H.-S.; Ma, J.; Sattar, S.; Hafiz, S. B.; Mahfuz, M. M. A.; et al. Peel-and-Stick Integration of Atomically Thin Nonlayered PtS Semiconductors for Multidimensionally Stretchable Electronic Devices. *ACS Appl. Mater. Interfaces* **2022**, *14* (17), 20268-20279

(39) Yang, S.; Ng, E.; Lu, N. Indium Tin Oxide (ITO) serpentine ribbons on soft substrates stretched beyond 100%. *Extreme Mech. Lett.* **2015**, *2*, 37-45

Table of Contents